IrO_x-Pt electrode for electro-oxidation of ethanol for alkaline type direct ethanol fuel cell: An excellent CO-tolerant catalyst

Md. Fahamidul Islam [a, b], Jahir Ahmed [c, d], M. Faisal [c, d], Jari S Algethami [c, d], Kentaro Aoki [e], Yuki Nagao [e], Farid A. Harraz [c, f, *], Mohammad A. Hasnat [a, *]

[a] *Electrochemistry & Catalysis Research Laboratory (ECRL), Department of Chemistry, School of Physical Sciences, Shahjalal University of Science and Technology, Sylhet-3114, Bangladesh*

[b] *Department of Chemistry, Faculty of Science, Noakhali Science and Technology University, Noakhali-3814, Bangladesh*

[c] *Promising Centre for Sensors and Electronic Devices (PCSED), Advanced Materials and Nano Research Centre, Najran University, Najran 11001, Saudi Arabia*

[d] *Department of Chemistry, Faculty of Science and Arts, Najran University, Najran 11001, Saudi Arabia*

[e] *School of Materials Science, Japan Advanced Institute of Science and Technology, 1-1 Asahidai, Nomi, Ishikawa, 923-1292, Japan*

[f] *Department of Chemistry, Faculty of Science and Arts at Sharurah, Najran University, Sharurah 68342, Saudi Arabia*

**Corresponding author:*

Mohammad A. Hasnat, E-mail: mah–che@sust.edu,

Farid A. Harraz, E-mail: faharraz@nu.edu.sa

Abstract

In this study, iridium oxide layer deposited on Pt surface (IrO_x-Pt) was utilized to explore ethanol oxidation reaction (EtOR) in alkaline medium. To fabricate the catalyst, cleaned Pt surface was scanned from 0 V to +1 V vs. Ag/AgCl (sat. KCl) in $Ir_2O_3 \cdot xH_2O$ colloidal suspension for 10 incessant cycles. A cyclic voltammogram recorded in 0.1 M NaOH solution corroborated the presence of IrO_x by showing the appearance of a distinct redox pair on the Pt

surface, with E_{pa} at −0.31 V and E_{pc} at −0.27 V. Energy dispersive mapping verified the uniform deposition of IrOx on Pt, and X-ray photoelectron spectroscopy showed that IrO_x contains both Ir^{III} and Ir^{IV} species. The results of cyclic voltammetric analysis indicated that the activity of the pure Pt catalyst towards EtOR was approximately 1.3 times greater than that of IrO_x-Pt. However, the CO-tolerant ability of the Pt catalyst was roughly 3.5 times lower than that of IrO_x-Pt. The results of the stability test indicated that the current density associated with EtOR on the IrO_x-Pt electrode experienced a decrease of approximately 18% with a standard deviation of 1.15% after undergoing 500 consecutive cycles. In contrast, the Pt electrode exhibited a decrease in activity of nearly 50% with a standard deviation of 1.53% under similar experimental conditions. The study on scan rate dependence revealed that the electrode reaction was a process limited by mass transfer.

Keywords: *Iridium oxide; Pt electrode; CO tolerance; Ethanol oxidation reaction; Fuel cell.*

1. Introduction

The global reliance on fossil fuels has long been a matter of concern due to both the finite availability of these resources and their involvement in global warming. Energy experts have made a prediction based on current and anticipated future rates of fuel consumption that the depletion of fossil fuel reserves may occur by the turn of the twenty-first century.[1] Moreover, as a result of the substantial combustion of fossil fuels, the emission of greenhouse gases has escalated to an unprecedented level in the world. Consequently, the global temperature is increasing at an alarming rate, leading to catastrophic alterations in the climate.[2] Anthropogenic activities have caused a rise in global temperature of approximately 1.01 °C since 1880.[3,4] The Intergovernmental Panel on Climate Change (IPCC) has forecasted that there will be a rise in global temperature of around 1.5 °C between the years 2030 and 2050, should the current rate of increase persist.[4] Therefore, today's world is in dire need for alternative energy source to maintain the sustenance of human race. In the context of this concern, fuel cell technology, alongside renewable energy sources, has garnered significant global attention as it has the potential to effectively deliver clean and sustainable power.

In recent years, there has been significant interest in the use of liquid fuel-based fuel cells, specifically those utilizing alcohol, as a means of generating electricity.[5,6] The alcohol-based

fuel cell is generally recognised as direct alcohol fuel cell (DAFC) where simple alcohols are directly used as fuel. Among simple alcohols, methanol is preferred as fuel because it is cheap, abundant and easy to store.[5] But the venomous nature of methanol cannot be ignored as its exposure can cause lifelong blindness and even death.[7] Methanol-based fuel cell can also be dangerous as it is easily combustible and has low boiling point.[8] Given these possible risks, ethanol can be a perfect alternative to methanol because of its low toxicity and higher boiling point.[9,10] Meanwhile, methanol and ethanol are oxidized by releasing 6 and 12 electrons, respectively. Hence, energy density of ethanol is sufficiently larger than that of methanol.[11]

Direct ethanol fuel cell (DEFC) can be categorized into two types based on pH of electrolyte: (I) Acidic DEFC; (II) Alkaline DEFC.[9] Generally, alkaline type DEFC is preferred over acidic type because: (I) higher [OH^-] enhances the kinetics of EtOR; (II) metals other than platinum (Pt) e.g., palladium (Pd), gold (Au), silver (Ag), show good catalytic activity in EtOR.[9,11–17] The suitability of Pt as an anode material, and also as a cathode material, for fuel cells such as DEFC, methanol fuel cells, hydrogen fuel cells, etc. is widely recognized.[9,18–20] However, its efficacy tends to diminish over time due to the irreversible adsorption of intermediate species, specifically carbon monoxide (CO) in EtOR process, as previously reported.[9,18,21]

Several works have been conducted to get rid of CO poisoning and to increase catalytic activity of Pt catalyst. For instance, Fujiwara and others studied the ethanol oxidation reaction by co-electrodeposited Pt-Ru (ruthenium) electro-catalysts.[22] Their investigation revealed that the presence of Ru facilitates the reaction between chemisorbed species, specially adsorbed CO and the oxidant. Hasan *et al.* developed a series of anode materials based on Pt, Pd and poly 1,8-diaminonapthalene to investigate EtOR in alkaline medium**.**[23] To prepare the catalysts, they firstly conducted electro-polymerization experiment to modify GC by poly1,8-diaminonaphthalene and the resultant electrode was then modified with single and bimetallic Pt, Pd via electro-deposition method. Among the developed catalysts, bimetallic system in combination with poly 1,8-diaminonaphthalene, was reported to be superior in terms of current density, onset potential, long term stability and most importantly, CO tolerance. To enhance the performance of Pt in EtOR, Du and co-workers synthesised core-shell type nano-alloy of Pt and SnO_2 (tin oxide) via polyol method.[24] According to their research, incorporation of SnO_2 nanoparticles promotes C–C bond splitting of ethanol on Pt catalyst and consequently, complete oxidation of ethanol was increased by at least three times than that on Pt. Again, Lui *et al.* developed monodisperse and homogeneous Pt_3Sn nanoparticles via co-reduction of Pt and Sn salts in organic solution to promote complete oxidation of ethanol.[25] Li and colleagues

conducted research aimed at enhancing the selectivity of the C1 pathway, specifically with regards to the cleavage of C–C bonds in ethanol.[26] Firstly, they fabricated carbon supported anode materials consisting of SnO_2 centre embellished with bimetallic composites of Pt, Ir (iridium) and Rh (rhodium). Among the anode materials, they found Pt/Ir bimetallic combination as effective catalyst for complete oxidation of ethanol via promoting C1-pathway. They also found that high loading of Ir metal reduced onset potential of EtOR and increased selectivity of C1-pathway. For DEFC, Ribeiro *et al.*[27] and Tayal *et al.*[28], independently synthesised a series of carbon supported catalysts where they incorporated Ir and Sn to enhance the activity of Pt. Both groups found the ternary combination of Pt, Ir and Sn as the most effective catalyst for EtOR in terms of current density and CO tolerance. Note that both groups used different route to synthesize the catalysts. Ribadeneira *et al.* investigated EtOR at 323 K by means of Pt-based bimetallic and trimetallic catalysts supported on carbon.[29] They used alcohol reduction process to prepare array of catalyst based on Pt, Ru, Sn and Ni (nickel) metals for DEFC. In terms of ethanol oxidation current density, trimetallic combination of Pt, Ru, and Ni showed superior response. Fang *et al.* developed Ir alloyed Pt nanorods for the purpose of studying EtOR.[30] Their findings revealed a noteworthy faradic efficiency of 61.21% for the C1 pathway and a remarkable ability to tolerate against CO adsorption.

The preceding discourse indicates that the process of alloying or modifying Pt with other transition metals, such as Sn, Ru, and Ir, is commonly employed to enhance the resistance of the Pt catalyst to CO adsorption. The prevailing theory regarding the alloying of Pt with Sn, Ru, and Ir posits that these metals adsorb OH^- ions, which serves as an oxidizing agent for adsorbed CO on Pt.[31–34] Moreover, Sn and Ir have a weakening effect on the Pt-CO bond through the downshift of the d band of Pt.[24,25,28] Sn and Ru based Pt composites are widely utilized as CO tolerant anode material, but their preparation in most of the case is a lengthy process that requires the use of sophisticated instruments. The dissolution of these catalysts during prolonged cycling is also a limitation, as acknowledged in literature by Ridgon *et al.*[33] With regards to the metal Ir, it is evident in earlier discussion that alloying with Pt enhance the CO tolerance and ethanol oxidation ability of Pt. But the utilisation of Ir metal without associating with Pt or other metals exhibits the CO poisoning phenomenon during EtOR.[9] Despite this fact, the Ir metal or its oxide, particularly IrO_2, has been utilized directly in EtOR or to enhance the performance of other catalyst like Pt, Sn, Ru, RuO_2 in EtOR.[30,35–41] Furthermore, the utilization of Ir metal oxide as an electrode material has been investigated for various applications, including the oxidation of organic molecules,[42,43] oxygen evolution

reaction,[44–53] oxygen reduction reaction,[50] pH sensing.[54] According to reports, Ir species, particularly iridium oxide, exhibit a high degree of stability in various aqueous environments and do not experience corrosion.[42,43] As far as current knowledge extends, the potential of mixed oxide of Ir, that is IrO_x, has yet to be fully investigated as a viable option for anode material in alcohol-based fuel cells, particularly in terms of its CO-tolerant properties. As previously stated, oxophilic metals are employed to attenuate the Pt–CO bond, leading to the displacement of adsorbed CO from Pt sites and/or promoting the oxidative elimination of CO.[25] It is also pertinent to note that the presence of oxygen-containing materials significantly enhances the kinetics of EtOR in an alkaline condition.[21] Since IrO_x is an oxygen-rich material, so it has the potential to serve as a co-catalyst, specifically as a CO anti-poisoning agent for Pt in EtOR.

Therefore, we fabricated an IrO_x-Pt electrode by means of simple electro-deposition technique to investigate EtOR. Primarily, the fabricated electrode was subjected to characterization through the use of cyclic voltammetric method. In addition, the surface morphology and chemical composition were analyzed utilizing a scanning electron microscope (SEM) in conjunction with energy dispersive X-ray spectroscopy. Subsequently, the voltammetric method was employed to assess the catalytic efficacy, CO-tolerance capacity, and certain kinetic information of EtOR on the fabricated electrode.

2. Experimental

2.1. Chemicals

Potassium hexachloroiridate (K_2IrCl_6), ethanol (C_2H_5OH), sodium hydroxide (NaOH), sulphuric acid (H_2SO_4), and hydrochloric acid (HCl) are the chemicals that were used to conduct all the experiments. These chemicals were purchased from Sigma Aldrich and used without further refining.

2.2. Synthesis of $Ir_2O_3.nH_2O$ colloidal suspension

Following the synthetic route established by Baur et al., K_2IrCl_6 was used to prepare colloidal solution of $Ir_2O_3 \cdot xH_2O$.[55] The synthesis process is shortly described below:

The process was initiated through dissolving 0.13 g of K_2IrCl_6 in 10 mL 0.1 M HCl solution by maintaining 90–105 °C temperature for around 60 minutes. Once the solution was prepared, absolute C_2H_5OH of 1.5 mL was added and gently boiled the mixture at around 105 °C temperature with moderate agitation. To maintain constant volume, required amount of

deionized water was added at the time of boiling. After boiling the solution at around 105 °C temperature for 120 minutes, 100 μL of absolute C_2H_5OH was again added to the solution. Maintaining 10 minutes time interval, the addition of C_2H_5OH was taken place until the colour of the solution changed from reddish black to clear blue. And the addition was continued to the point where blue colour remained unchanged upon further addition of ethanol. It should be noted that the boiling temperature, around 105 °C, was maintained during the addition of C_2H_5OH. After that, we carried on boiling for another 60 minutes to remove excess C_2H_5OH. After vaporization, the heat source was turned off and the resultant solution was left at room temperature to cool down. Finally, 0.5 M NaOH solution was carefully added until the pH value reached at 12.0. Note that, N_2 environment was maintained during NaOH addition. The resultant colloidal solution of $Ir_2O_3.xH_2O$ was then used to modify electrode.

2.2. Electrochemical experiments and electrode fabrication

Electrochemical workstations *e.g.*, CHI 660E (CHI Instruments, USA) and Autolab PGSTAT128N were used to conduct all the electrochemical investigations. The electrochemical experiments were conducted in a one-compartment electrochemical cell configured with conventional three-electrode system, where a Teflon coated polycrystalline Pt electrode having diameter of 3 mm was served as working electrode, Pt wire was used as auxiliary electrode and Ag/AgCl (sat. KCl) was served as reference electrode. To ensure contamination-free surface, Pt electrode was gone through a series of treatments. The cleansing process was initiated through polishing the Pt surface with alumina slurry (0.03 μm) for 10 minutes. Then, the electrode was properly washed with deionized water and sonicated in 0.1 M H_2SO_4 solution for 10 minutes. At that point, the electrode was voltammetrically activated though repeated cycling in the potential range of −0.2-1.5 V (vs. Ag/AgCl (sat. KCl)) at 0.1 V s^{-1} scan rate for 20 minutes.

Electrodeposition method was used to immobilise IrO_x layer on Pt electrode surface. In this method, the contamination-free Pt surface was placed in the colloidal solution of $Ir_2O_3.xH_2O$ and scanned in the potential range of 0.0 to 1.0 V (vs. Ag/AgCl (sat. KCl)) at 0.1 V s^{-1} for 10 repeated cycles. After that, the resultant electrode, denoted as IrO_x-Pt, was scanned in 0.1 M NaOH solution to confirm the presence of IrO_x layer on Pt surface.[55] Finally, the Pt and IrO_x-Pt electrodes were utilized as working electrode to explore the ethanol oxidation reaction (EtOR) in 1.0 M NaOH. Note that, inert atmosphere was maintained though purging N_2 gas under room temperature (25 ± 2 °C).

2.3. Characterization

The oxidation states of chemical components and chemical composition of IrO_x-Pt were investigated by X-ray photoelectron spectroscopy (XPS) using a delay-line detector (DLD) spectrometer (Kratos Axis-Ultra; Kratos Analytical Ltd.) with an Al *K*α radiation source (1486.6 eV). The conductive carbon tape was used to attach the sample, and each spectrum was calibrated to the C 1*s* peak at 284.8 eV as the inner reference. Obtained spectra were fitted using XPSPEAK 4.1 software with the subtraction of the background by Shirley method. In case of bare Pt surface, the valence and chemical states were determined using a methodology analogous to that employed for the IrO_x-Pt catalyst.

The surface morphology and the chemical composition of IrO_x-Pt were characterized through a scanning electron microscope (SEM) coupled with energy dispersive X-ray spectroscopy (EDX, TM3030Plus miniscope; Hitachi Ltd.). The conductive carbon tape was used to attach the sample, and the images were taken with the irradiation voltage of 15 keV. In addition, SEM) imaging and EDX investigations have been carried out on the unmodified Pt surface using a procedure similar to that employed for the IrO_x-Pt catalyst.

3. Results and Discussion

3.2. Fabrication of IrO_x-Pt electrode

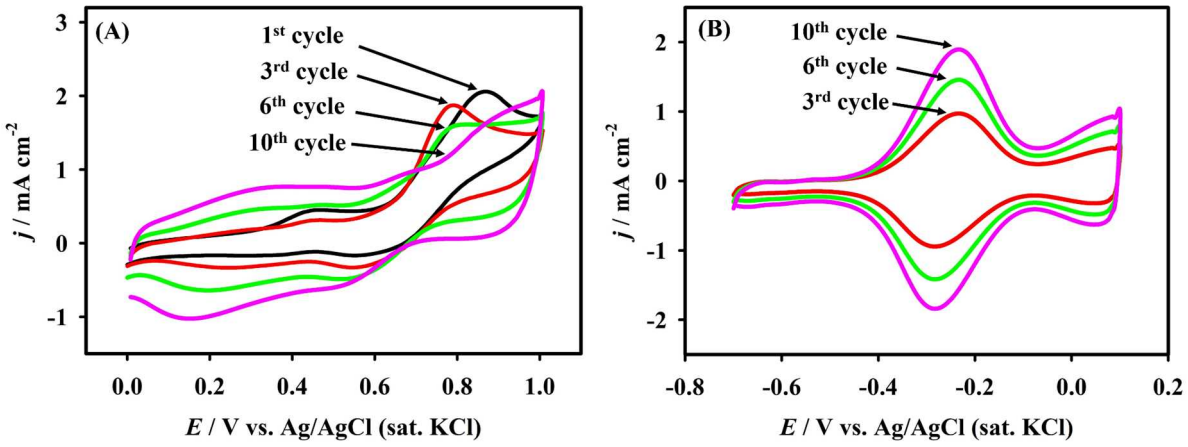

Figure 1. (A) Cyclic voltammograms of IrO_x film growth on Pt electrode obtained in $Ir_2O_3.xH_2O$ colloidal solution by incessant scanning from 0 V to +1.0 V for 10 cycles at 0.1 V s^{-1} scan rate, (B) Characteristic cyclic voltammograms of developed IrO_x-Pt surface in 1.0 M N_2-saturated NaOH at 0.1 V s^{-1} after each three deposition cycles.

Cyclic voltammetric technique was used to deposit IrO_x onto Pt electrode surface. To do this, a clean Pt electrode was placed in a one-compartment electrochemical cell containing $Ir_2O_3 \cdot xH_2O$ colloidal solution and was then repeatedly scanned from 0 to +1 V against Ag/AgCl (sat. KCl) at scan rate 0.1 V s^{-1}. For optimal surface coverage, the deposition scan was limited to 10th cycle as per report of Baur *et al.*[55] The obtained cyclic voltammograms concerning the development of IrO_x onto Pt surface are shown in **Fig. 1(A)**. According to Baur et al. the peak at *ca*. 0.87 V (vs. Ag/AgCl (sat. KCl)) in 1st cycle belong to generation of oxygen from hydroxide ion which gradually shifted and diminished in next cycles [55]. Additionally, the gradual current increment and the development of redox waves in the potential range of 0 V to +0.6 V (vs. Ag/AgCl (sat. KCl)) reflects the formation of iridium oxide layer onto Pt surface. According to Baur et al. the iridium oxide undergoes oxidation reaction on Pt surface during positive potential scanning and the reaction (1) also takes place on the Pt electrode surface to form insoluble layers of iridium oxide.[55]

$$Ir_2O_3.xH_2O + 2OH^- \rightleftharpoons 2IrO_2.xH_2O + H_2O + 2e^- \qquad (1)$$

To perceive of the loading of iridium oxide layer, the Pt electrode was transferred to basic solution after every three deposition cycles and was scanned in potential range of −0.7 V to 0 V vs. Ag/AgCl (sat. KCl) at 0.1 V s^{-1} scan rate. **Figure 1(B)** represents the resultant cyclic voltammograms recorded in N_2-saturated 1.0 M NaOH solution. It is seen from this figure that a distinct redox pair is appeared on the Pt surface displaying anodic peak potential, E_{pa}, at −0.31 V and cathodic peak potential, E_{pc}, at −0.27 V with respect to Ag/AgCl (sat. KCl). According to Rivera et al. this surface confined redox duo belongs to $Ir^{III}O_x/Ir^{IV}O_x$ [56]. The current associated with Ir^{III}/Ir^{IV} transition gradually intensified with the increment of deposition cycle and reached to optimal level at 10th deposition cycle. Therefore, the resultant IrO_x-Pt electrode after 10th deposition cycle was utilized for electrochemical oxidation of ethanol.

3.2. Characterization

To confirm the oxidation state and identify the chemical species of IrO_x, XPS was conducted. **Figure 2** shows the **(A)** Ir and Pt 4*f* and **(B)** O 1*s* XPS spectra before (black) and after (red) the IrO_x deposition on Pt electrode, respectively. After the deposition, peaks corresponding to IrO_x were observed in Ir 4*f* (**Fig. 2(A)**) and O 1*s* (**Fig. 2(B)**) regions, while peak positions of Pt $4f_{7/2}$ and $4f_{5/2}$ did not change before and after the deposition. The peak observed in O 1*s* region of Pt (black line in **Fig. 2(B)**) was probably assignable to oxygen components from surface adsorbed water or the carbon species. Obtained spectra were fitted well considering two

components in Ir 4*f* region and three components in O 1*s* region. Ir $4f_{7/2}$ and $4f_{5/2}$ peak positions (**Table S1**) were consistent with those of IrO_2 and Ir_2O_3, indicating that Ir^{III} and Ir^{IV} species coexist in IrO_x [57]. The Ir^{III}: Ir^{IV} ratio was estimated to be 0.30: 0.70 calculated from the deconvoluted peak area (**Table S1**). For O 1*s*, three peaks were assignable to the O^{2-}, OH^- and hydrating H_2O, respectively with the area ratio of O^{2-}: OH^-: (hydrating H_2O) = 0.46: 0.49: 0.05 (**Table S2**) [23,58]. A considerable amount of OH^- species exists, suggesting the partial replacement of O^{2-} to OH^- in Ir_2O_3 or IrO_2, leading to the formation of such species as IrO(OH) or $IrO(OH)_2$ [59,60].

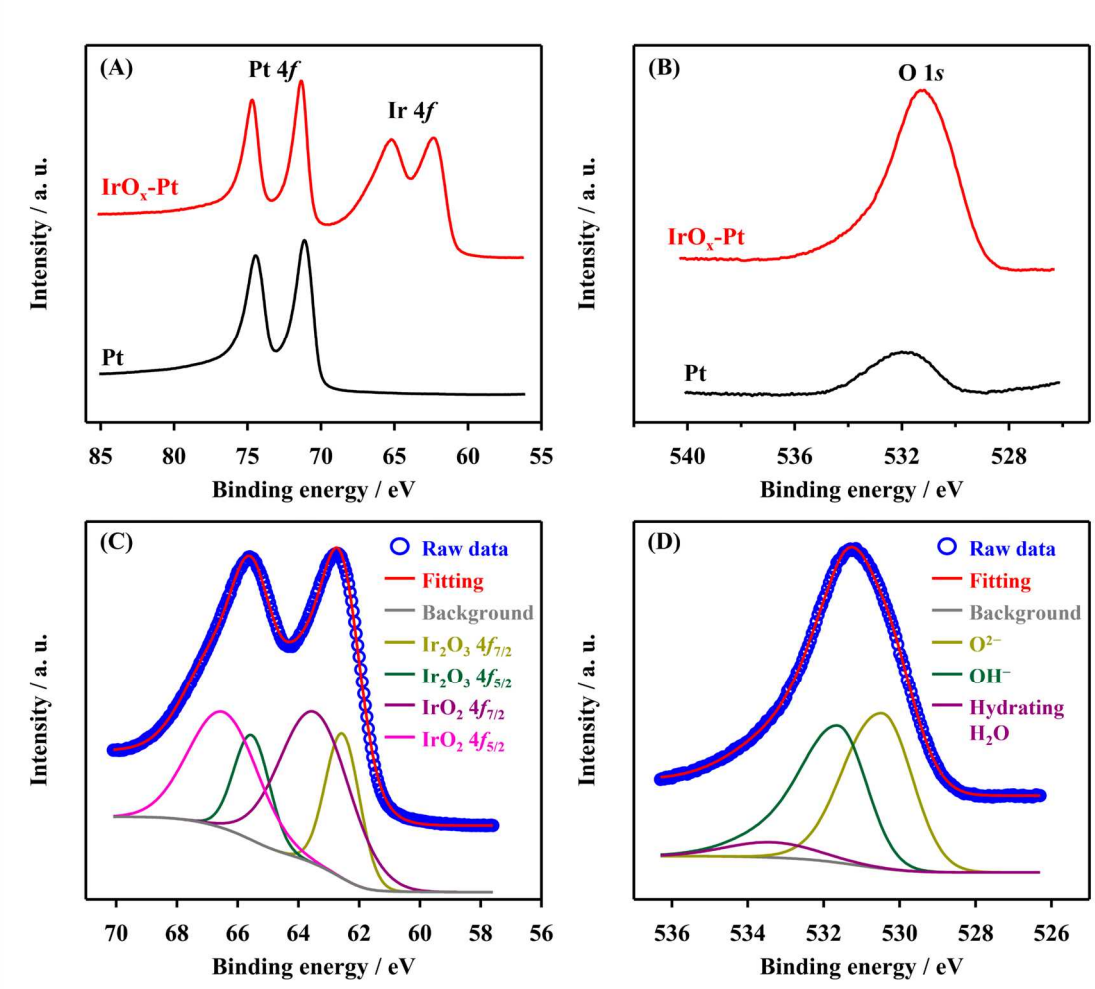

Figure 2. (A) and (B) XPS spectra of Pt (black) and IrO_x-Pt (red) in (A) Ir and Pt 4*f* regions and (B) O 1*s* region. (C) and (D) Fitting results of (C) Ir 4*f* and (B) O 1*s* XPS spectra of IrO_x-Pt electrode.

The surface morphology and the chemical composition of the IrO_x-Pt electrode were investigated by SEM and EDX. **Figure 3** shows the SEM images **(A)** before and **(B)** after the

electrochemical deposition of IrO_x on Pt electrode. After the deposition, particles up to 10 µm were observed on the Pt surface. It was clearly confirmed from 2D EDX mappings of IrO_x-Pt electrode (**Fig. 3(C)** and **(D)**) that Ir and O distribute almost uniformly on Pt electrode. EDX spectra (**Fig. S1**) indicated that only Ir and O exist on Pt-electrode after the deposition, with Ir and O contents of 3.12 and 34.06 atomic%, respectively (**Table S3**). It is worth noting that the oxygen content was much higher than that expected from IrO_2 or Ir_2O_3. Excess oxygen was probably derived from the hydration water or the replacement of O^{2-} to OH^-, as revealed from XPS results.

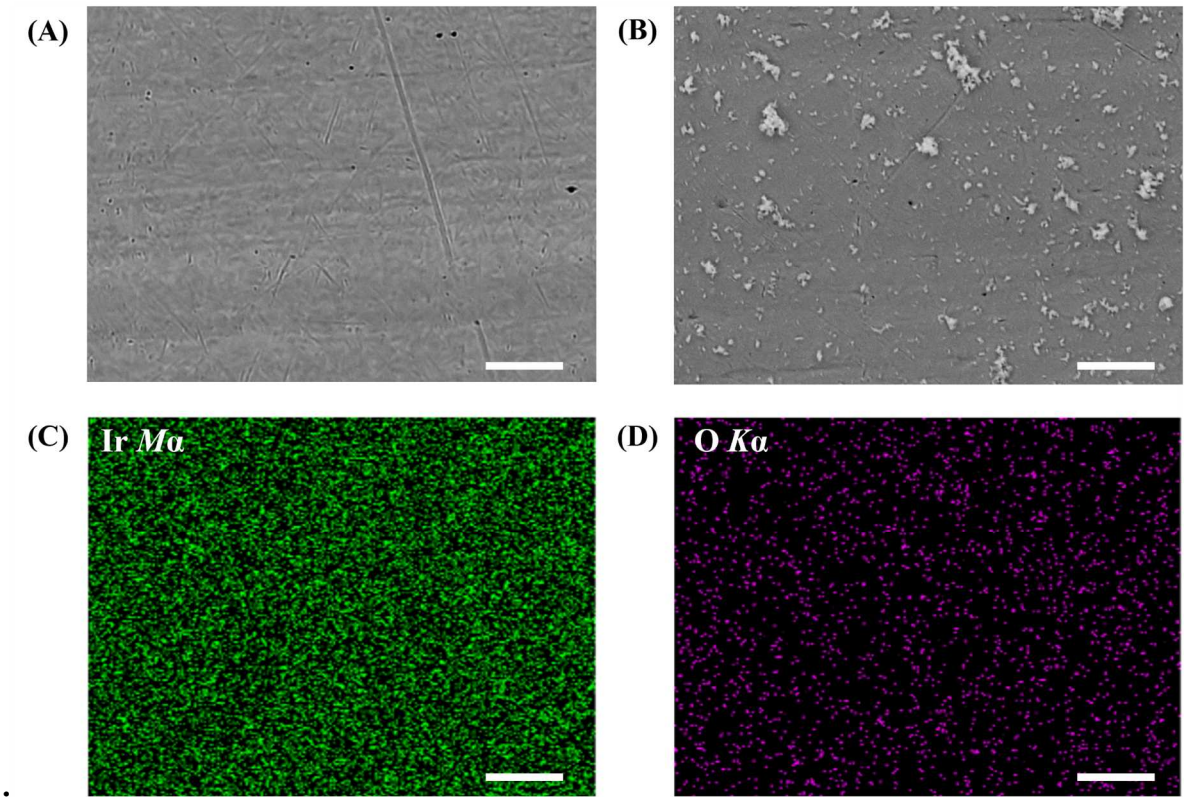

Figure 3. (A) and (B) SEM images of (A) Pt and (B) IrO_x-Pt electrodes. (C) and (D) 2D elemental mapping of (C) Ir and (D) O with the same field of view as (B). Scale bar: 5 µm for all panels.

3.3. Electrochemical characterisation of IrO_x-Pt

To examine the properties of the IrO_x-Pt electrode, electrochemical experiments were also carried out. In 1.0 M N_2-saturated NaOH solution, bare Pt shows the voltammogram as given in **Fig. 4(A)**. According to Banik et al., the voltammogram of bare Pt in NaOH solution can be divided into three regions with the exclusion of the potential region where hydrogen evolution reaction takes place.[61] The first region (denoted as Region-I), which is in between −0.7 to −0.48

V vs. Ag/AgCl (sat. KCl), corresponds to desorption (forward scan) and adsorption (reverse scan) of H^+ ions on Pt electrode surface as per reaction (2).[61]

$$Pt - H + OH^- \rightleftharpoons Pt + H_2O + e^- \quad (2)$$

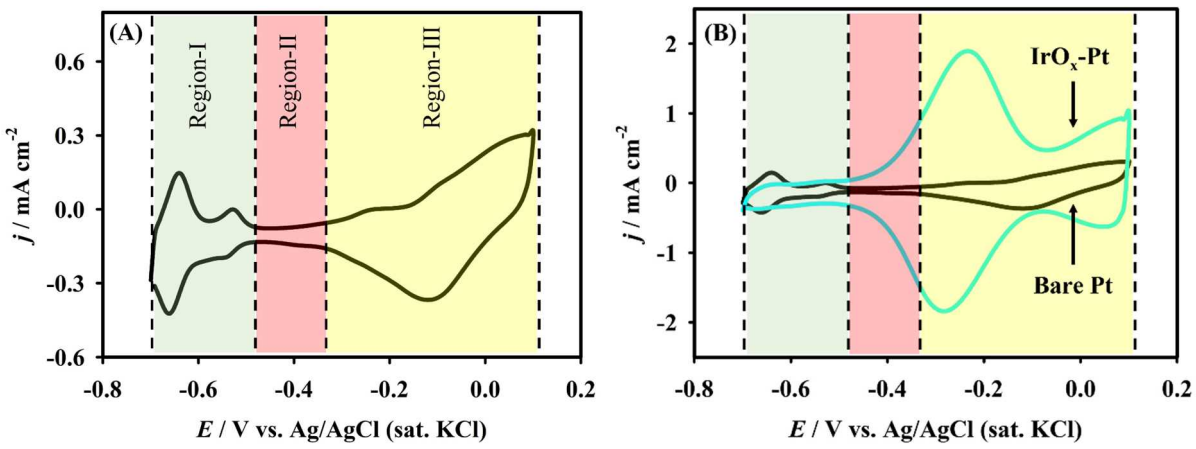

Figure 4. (A) Cyclic voltammogram of bare Pt surface obtained in 1.0 M N_2-saturated NaOH solution at scan rate of 0.1 V s^{-1}, (B) Cyclic voltammograms of both bare Pt and IrO_x-Pt electrodes in 1 M N_2-saturated NaOH solution at scan rate of 0.1 V s^{-1}.

Region-II (−0.5 to −0.34 V) is considered as 'double-layer region' where only capacitive current is observed.[61] Lastly, the region beyond −0.34 V (vs. Ag/AgCl (sat. KCl)) is denoted as Region-III where adsorption of OH^- ions on Pt surface is observed in forward scan and the corresponding reverse reaction is found at *ca.* −0.12 V (vs. Ag/AgCl (sat. KCl)) as per reaction (3).[61]

$$Pt + OH^- \rightleftharpoons Pt(OH)_{ads} + H_2O + e^- \quad (3)$$

However, it is seen from **Fig. 4(B)** that the characteristic feature of Pt electrode vanished after immobilisation of IrO_x on the Pt surface. At the same time, a distinct redox duo displaying E_{pa} at −0.31 V and E_{pc} at −0.27 V (vs. Ag/AgCl (sat. KCl)) was seen to appear in 1.0 M NaOH solution. Therefore, the appearance of redox wave confirmed the formation of IrO_x layer on Pt surface.

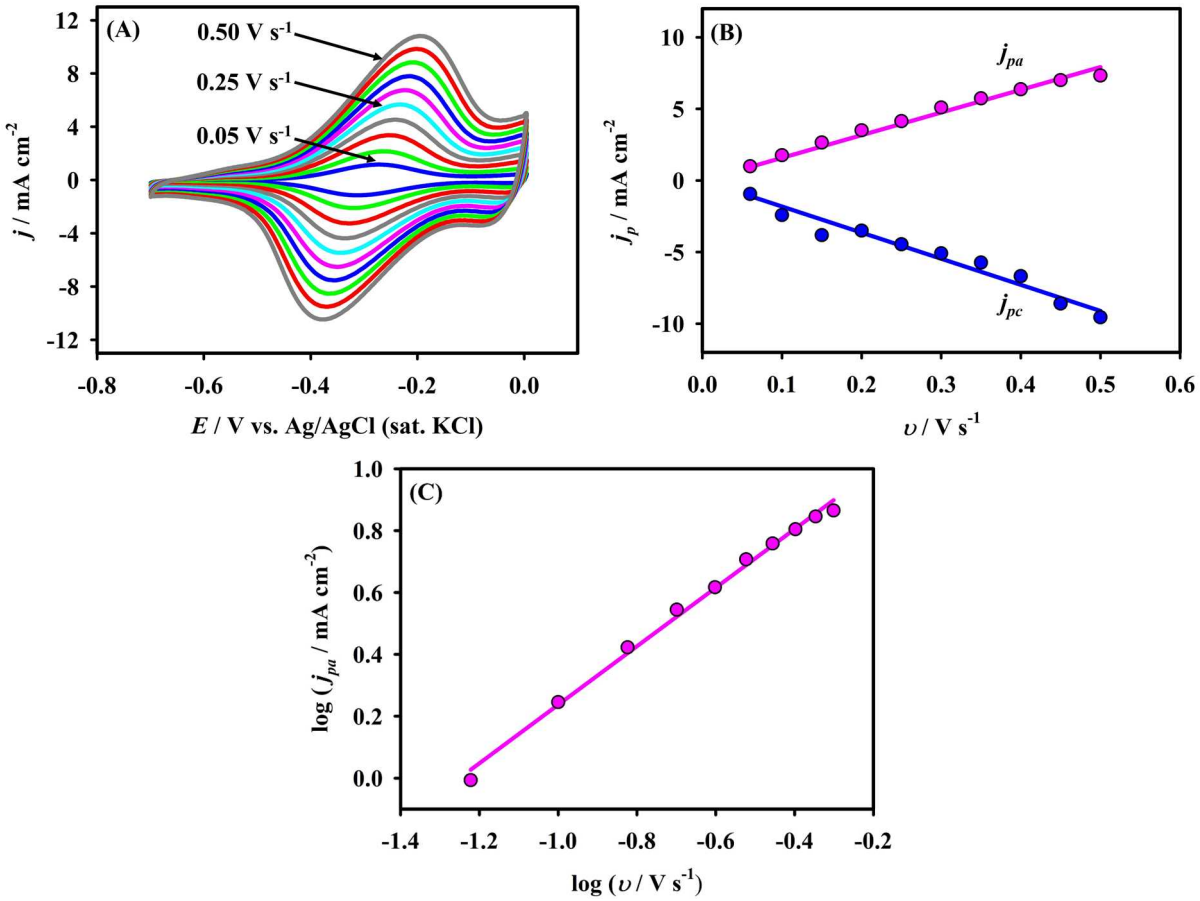

Figure 5. (A) Scan rate dependent cyclic voltammograms of IrO_x-Pt electrode in 1.0 M N_2-saturated NaOH solution, (B) Linear relationship between peak current densities of redox waves and scan rates, (C) Logarithmic relationship between anodic peak current densities and scan rates.

To evaluate several features of IrO_x layer, the scan rate dependent cyclic voltammograms were recorded by utilizing the IrO_x-Pt electrode in 1.0 M N_2-saturated NaOH solution. From the **Fig. 5(A)**, it is clear that both anodic and cathodic peak current density increased with the increment of scan rate from 0.05 to 0.50 V s^{-1}. The nature of CVs in scan rate study remained unaltered on subsequent potential scanning suggesting that the IrO_x layer was unwaveringly attached to the Pt surface [62]. Therefore, to estimate average surface concentration (Γ) of IrO_x on Pt surface, the peak current densities (both anodic and cathodic) were plotted against variable scan rates as per equation (4),[63,64] which formed straight lines having r^2 : 0.99 (see **Fig. 5(B)**)

$$j_p = \frac{n^2F^2\Gamma\upsilon}{4RT} \qquad (4)$$

Where, j_p stands for peak current density (anodic or cathodic), n stands for number of electron transfer (in this case, n = 1), F stands for the Faraday's constant (96485 C mol^{-1}), Γ represents

average surface concentration, υ stands for scan rate, R represents molar gas constant (8.314 J K^{-1} mol^{-1}), T represents temperature (298 K). Therefore, the active IrO_x species concentration (Γ) was calculated to be $(1.81 \pm 0.13) \times 10^{-8}$ mol cm^{-2}.

3.4. Electro-oxidation of ethanol

Typical cyclic voltammograms of EtOR on bare Pt and IrO_x-Pt electrodes are presented in **Fig. 6(A)**. Note that the reaction medium was 1 M N_2-saturated NaOH solution. It is seen from the figure that the voltammogram regarding EtOR has imperfect hysteresis loop lying in the potential range of −0.4 to 0.0 V with respect to Ag/AgCl (sat. KCl). For Pt electrode, the loop consists of intense anodic and cathodic oxidation waves at *ca.* −0.16 V and −0.21 V, respectively. The forward going wave was obtained for ethanol oxidation, whereas the wave found during reverse scan was due to the oxidation of adsorbed intermediate species, mainly CO, formed in anodic scan [18].

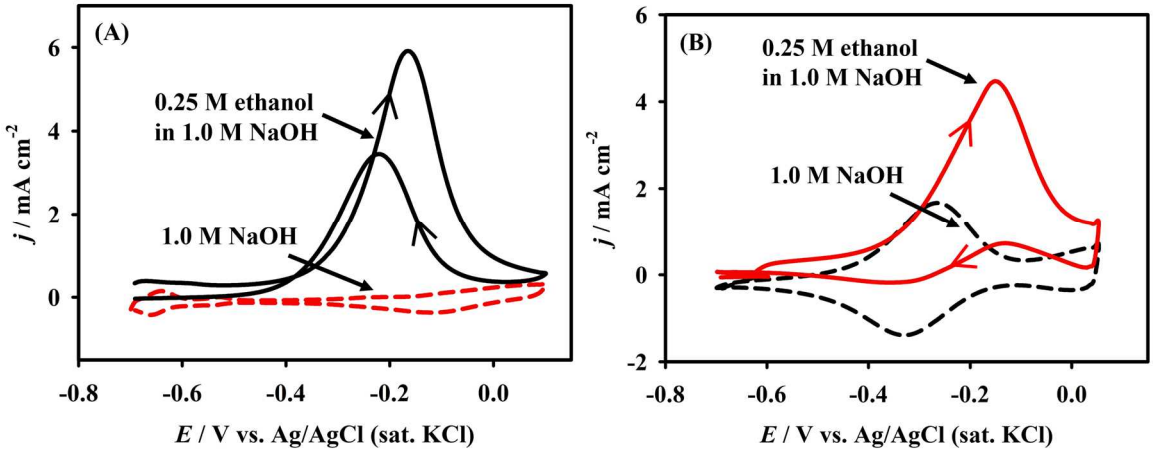

Figure 6. (A) Cyclic voltammograms of bare Pt in 1.0 M N_2-saturated NaOH solution having 0.0 M and 0.25 M ethanol at 0.1 V s^{-1} scan rate, (B) Cyclic voltammograms of IrO_x-Pt in 1.0 M N_2-saturated NaOH solution having 0.0 M and 0.25 M ethanol at 0.1 V s^{-1} scan rate.

In case of IrO_x-Pt electrode, both anodic and cathodic waves are less intense compared to the waves obtained for Pt electrode, as shown in **Fig. 6(B)**. On top of that the peak potentials of the forward and backward waves have also been shifted towards positive direction due to presence of IrO_x layer on Pt surface. But the onset potential of EtOR on Pt and IrO_x-Pt electrode is almost identical and interestingly, the onset potential of CO oxidation reaction on IrO_x-Pt electrode is also like that on bare Pt electrode. This observation leads to the conclusion that the Pt surface plays the main role in the electrocatalysis of ethanol. At this point, it seems that the

IrO_x layer impeded rather than promoting the catalytic activity of the Pt surface. However, the forward to backward peak current density ratio (j_{pf}/j_{pb}) reveals an intriguing property of electro-catalysts, namely their tolerance to the build-up of adsorbed intermediate species produced by EtOR.[15,23] Therefore, the ratio of j_{pf} and j_{pb} was calculated from the respective EtOR cyclic voltammograms and plotted with respect to the electro-catalyst (See **Fig 6(A) & (B)**). It is seen that the IrO_x-Pt has higher tolerance ratio compared to Pt, signifying the higher resistance to accumulation of adsorbed intermediate species on catalytic sites (See **Fig. S4**).

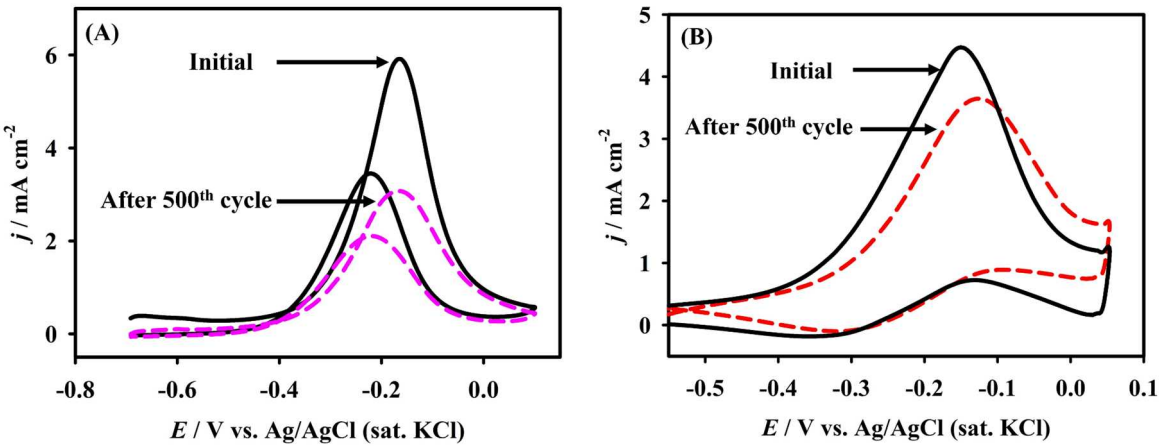

Figure 7. (A) Comparative cyclic voltammograms of bare Pt in 1.0 M N_2-saturated NaOH solution having 0.25 M ethanol at 0.1 V s^{-1} recoded initially and after 500 incessant cycling in 0.25 M ethanol solution, (B) Comparative cyclic voltammograms of IrO_x-Pt in 1.0 M N_2-saturated NaOH solution having 0.25 M ethanol at 0.1 V s^{-1} recoded initially and after 500 incessant cycling in 0.25 M ethanol solution.

To validate the tolerance ratio, stability test of the electrodes was taken place in 1.0 M NaOH solution containing 0.25 M ethanol. **Figure 7(A)** represents the comparison of CVs of Pt electrode, taken initially and after 500 incessant cycles in 0.25 M ethanol solution at scan rate of 0.1 V s^{-1}. It is obvious from the figure that the peak current density decreased by around (50±1.53) % after 500 cycles. Such current fall is a clear indication of Pt surface deactivation, which is consistent with the tolerance ratio of Pt. According to Lai *et al.*, the main reason behind the deactivation is adsorption of intermediate species, mainly CO, which form strong bond with Pt atoms and keeps the Pt surface unexposed to ethanol molecules.[18] On the contrary, the initial current response of IrO_x-Pt electrode dropped by (18±1.15) % after 500 incessant cycles in 0.25 M ethanol at scan rate of 0.1 V s^{-1}. This result clearly indicates that the IrO_x layer protects the Pt surface from unwanted accumulation of intermediate species. Furthermore, the stability test was performed for two more times to validate the primary data and almost

similar results were obtained. To make it easily apprehensible, the comparison between the initial peak current density and final peak current density (obtained after 500 cycles) was plotted with respect to the respective electrode, known as bar diagram, (See **Fig. S5**). Based on the results of the stability test and prior literature, it has been observed that the accumulation of adsorbed CO on the active sites of Pt leads to the deactivation of the Pt catalyst in the course of the EtOR process. (See scheme 1). As a result, the current response rapidly decreases upon subsequent cycling in ethanol solution.

Next, the data presented in **Table 1** is intended to provide a thorough comparison of the durability and resistance to CO adsorption exhibited by Pt-metal oxide catalysts that have been previously documented. It is obvious that the catalyst we developed is capable of oxidizing ethanol with appreciable longevity while also showing outstanding CO adsorption resistance.

Table 1. A comparative representation of relevant parameters for EtOR on varying Pt-Metal Oxide catalysts

Catalyst	Condition	j_{pf} and υ	j_{pb} and υ	j_{pf}/j_{pb}	Durability	b	Ref
Pt-CeO_2/C	1.0 M ethanol + 1.0 M KOH at 30 °C	19 mA cm^{-2} at 0.05 V s^{-1}	12 mA cm^{-2} at 0.05 V s^{-1}	1.6	–	–	65
Pt-ZrO_2/C	1.0 M ethanol + 1.0 M KOH at 25 °C	27 mA cm^{-2} at 0.05 V s^{-1}	25 mA cm^{-2} at 0.05 V s^{-1}	1.1	–	117 mV dec^{-1}	66
Pt-RuO_2/C/BDD	1.0 M ethanol + 0.5 M H_2SO_4 at 25 °C	72 mA mg^{-1} Pt at 0.01 V s^{-1}	80 mA mg^{-1} Pt at 0.01 V s^{-1}	0.9	Produced 33 % of the initial current density after 2500 s	140 mV dec^{-1}	67
SnO_2@Pt/C	1.0 M ethanol + 0.5 M H_2SO_4 at 25 °C	265 mA mg^{-1} Pt at 0.05 V s^{-1}	215 mA mg^{-1} Pt at 0.05 V s^{-1}	1.23	Produced 17 % of the initial current density after 600 s	–	68
Pt-ATO/MWCNT	1.0 M ethanol + 1.0 M H_2SO_4 at 25 °C	1300 mA mg^{-1} Pt at 0.05 V s^{-1}	1000 mA mg^{-1} Pt at 0.05 V s^{-1}	1.30	Produced 37 % of the initial current density after 3600 s	–	69

Ni@NiO/Pt	1.0 M ethanol + 0.5 M KOH at 21 °C	125 mA cm^{-2} at 0.02 V s^{-1}	100 mA cm^{-2} at 0.02 V s^{-1}	1.25	Produced 20 % of the initial current density after 3600 s	87 mV dec^{-1}	[70]
Pt-CeO_{2-x}/GNS	1.0 M ethanol + 1.0 M KOH at 25 °C	1370 mA mg^{-1} Pt at 0.05 V s^{-1}	220 mA mg^{-1} Pt at 0.05 V s^{-1}	6.23	94.9 % current density retention after 250 cycles	140 mV dec^{-1}	[71]
1Pt-3CuO/CNT	0.5 M ethanol + 0.5 M H_2SO_4 at 25 °C	596 mA mg^{-1} Pt at 0.05 V s^{-1}	536 mA mg^{-1} Pt at 0.05 V s^{-1}	1.11	Produced 35 % of the initial current density after 3600 s	108 mV dec^{-1}	[72]
Pt/TiO_2NCs-C	1.0 M ethanol + 0.5 M H_2SO_4 at 25 °C	0.640 mA cm^{-2} at 0.05 V s^{-1}	0.600 mA cm^{-2} at 0.05 V s^{-1}	1.1	95 % current density retention after 70 cycles	–	[73]
Pt-MoO_3/C	1.0 M ethanol + 0.5 M H_2SO_4 at 25 °C	0.675 mA cm^{-2} at 0.02 V s^{-1}	0.418 mA cm^{-2} at 0.02 V s^{-1}	1.61	Produced 30% of the initial current density after 3600 s	120 mV dec^{-1}	[74]
IrO_x-Pt	0.25 M ethanol + 1.0 M NaOH at 25 °C	4.47 mA cm^{-2} at 0.1 V s^{-1}	0.75 mA cm^{-2} at 0.1 V s^{-1}	5.96	Around 82 % current density retention after 500 cycles	165 mV dec^{-1}	**This work**

j_{pa} = peak current density during forward scan; j_{pb}= peak current density during backward scan; υ = scan rate; b = Tafel slope; C = Carbon; BDD = Boron Doped Diamond; ATO = Antimony Tin Oxide; MWCNT = Multi-Wall Carbo Nano Tube; GNS = Graphene Nano Sheet; CNT = Carbo Nano Tube; NCs = Nano Cubes.

3.5. Scan rate effect

Essentially, the analysis of an electrochemical reaction with respect to scan rate enables an understanding of both its mechanistic and kinetic aspects. For a complicated reaction like the ethanol oxidation reaction, it is rather challenging to extract all the kinetic parameters using the scan rate effect, but we can accurately predict some of the mechanistic features. Therefore, cyclic voltammagrams were recorded at variable scan rates (0.05 to 0.6 V s^{-1}) for ethanol oxidation reaction, in which the concentration of ethanol was 0.25 M in 1.0 M NaOH (see **Fig. 8(A)**).

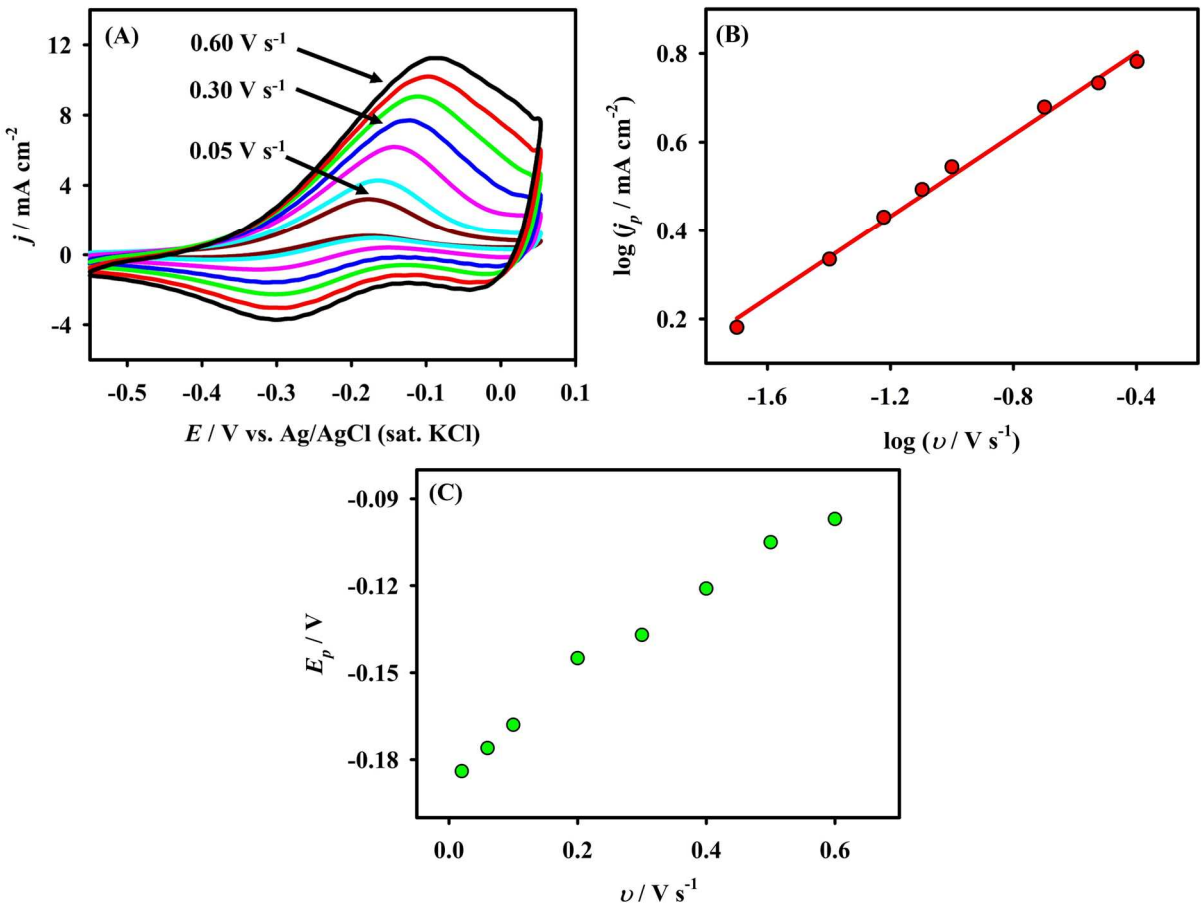

Figure 8. (A) Scan rate dependent cyclic voltammograms of IrO_x-Pt in 1.0 M N_2-saturated NaOH solution having 0.25 M ethanol, (B) Logarithmic relationship between anodic peak current densities and scan rates, (C) Variation of anodic peak potentials with respect to scan rates.

It is conspicuous in the figure that the peak current density increased in magnitude with increased scan rate. To know the nature of the electrode process, logarithmic peak current densities were plotted with respect to logarithmic scan rates, as shown in **Fig. 8(B)**. Linear regression analysis of the logarithmic plot yielded slope value of 0.46 (~ 0.5) with r^2:0.99, suggesting a diffusion-controlled electrode process.[75–77] The peak potential also shifted towards positive potential with the increase in scan rate, which is a sign of an irreversible electrode process (see **Fig. 8(C)**).[75–77]

3.6. Tafel analysis

At this point, Tafel slope can be a parameter to know the involvement of $Ir^{(III)}$ to $Ir^{(IV)}$ transition in catalysis of ethanol oxidation reaction.[78] By using the famous Tafel equation (5),[43] the analysis of the polarization curves in the potential region as marked by the dotted parallelogram

in **Fig. 9(A)** was performed for 1.0 M NaOH having 0.00 M, 0.15 M and 0.25 M ethanol as shown in **Fig. 9**(B)

$$\log j = \left\{ log\, j_k - \frac{E^0}{b} \right\} + \frac{E}{b} \qquad (5)$$

Where, $b = \frac{2.303RT}{(1-\alpha)F}$, known as Tafel slope for the anodic reaction, and the other symbols have their usual meanings.

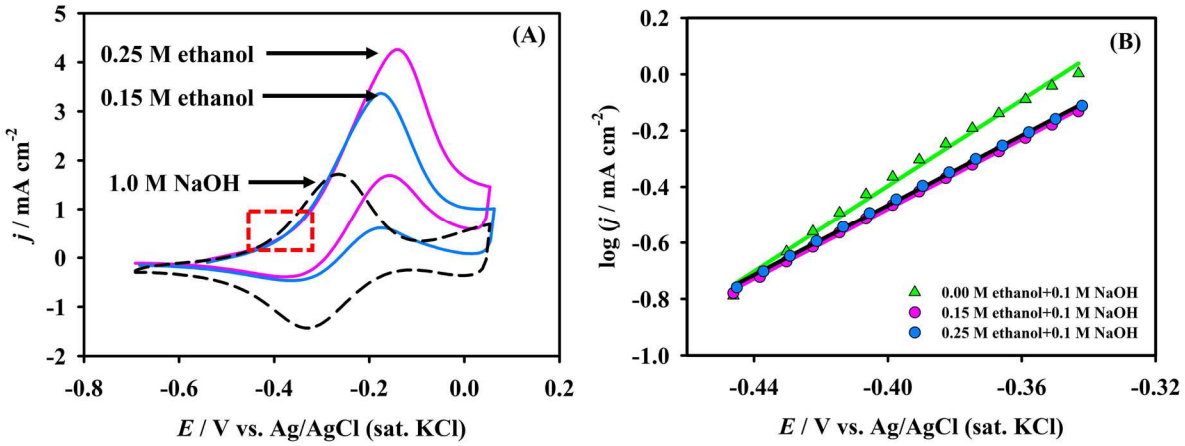

Figure 9. (A) Cyclic voltammograms of IrOx-Pt in 1.0 M N_2-saturared NaOH having 0.00 M, 0.15 M and 0.25 M ethanol at 0.1 V s^{-1}, (B) Tafel analysis of polarization curves of 1.0 M N_2-saturared NaOH having 0.00 M, 0.15 M and 0.25 M ethanol by using IrO_x-Pt electrode at 0.1 V s^{-1}.

In absence of ethanol in 1.0 M NaOH, the Tafel slope of IrO_x-Pt was found to be 130 mV dec^{-1} as per equation (5). Conversely, the Tafel slope of IrO_x-Pt was determined to be 165 mV dec^{-1} when exposed to 0.15 M and 0.25 M ethanol in a 1.0 M NaOH solution. The dissimilarity observed in the Tafel slope provides evidence that the transition from $Ir^{(III)}$ to $Ir^{(IV)}$ does not catalyse the EtOR,[78] Although the IrO_x layer does not contribute to catalysis, the findings depicted in **Figures 6 and 7** demonstrate that the IrO_x layer applied to the Pt catalyst functions as a layer that inhibits CO adsorption. Due to transition from $Ir^{(III)}$ to $Ir^{(IV)}$, IrO_x layer is inherently conductive. This transition occurs just before the oxidation of ethanol, therein the overall oxidation process is not impeded by IrO_x layer. Based on the obtained results and the theories stated in literatures [32–34], the overall oxidation process on IrO_x -Pt catalyst is shown in **Scheme 1**.

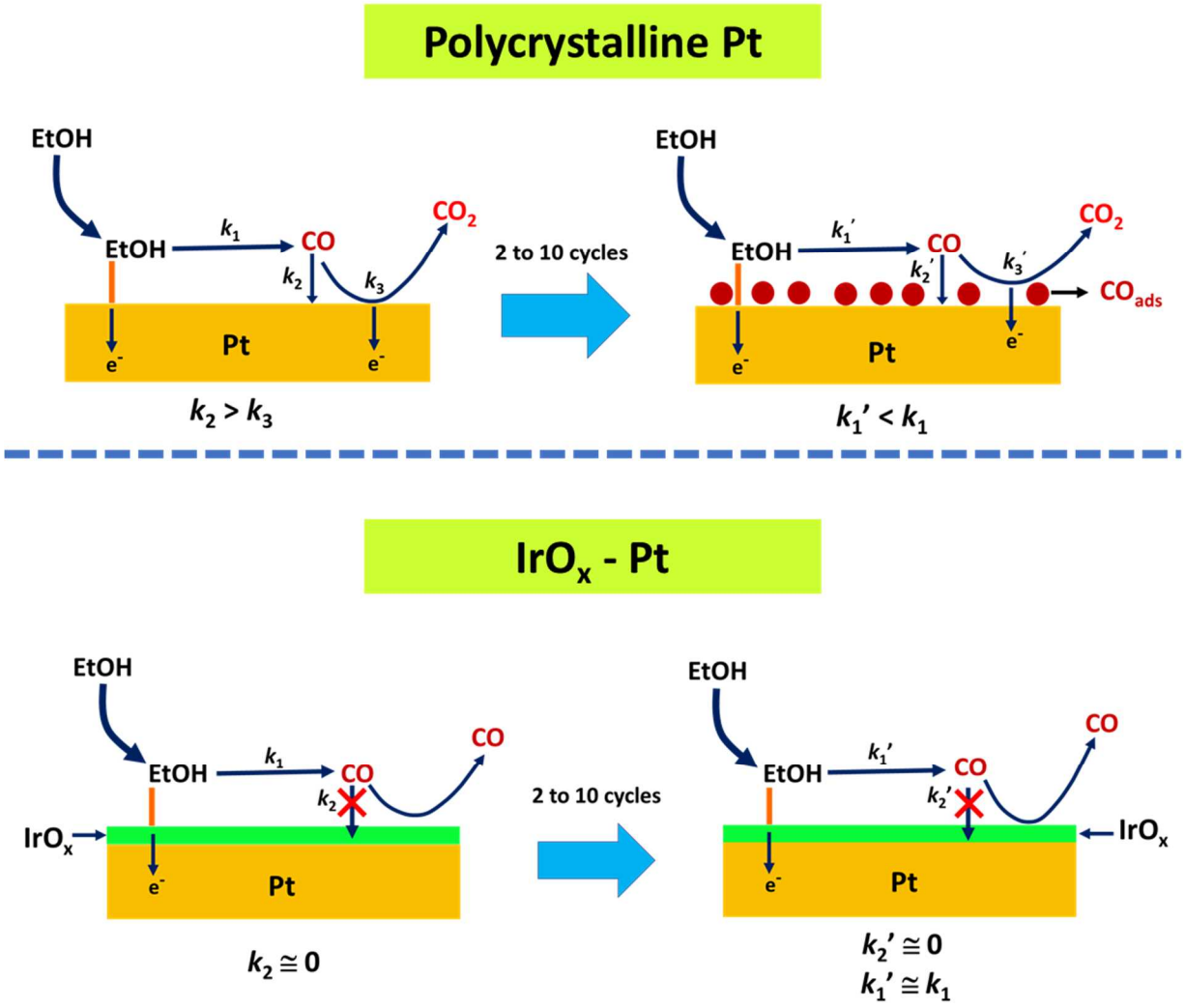

Scheme 1. Overall ethanol oxidation reaction on polycrystalline Pt and IrO_x-Pt.

4. Conclusion

The main purpose of this study is to make Pt surface CO tolerant in attaining EtOR for alkaline type DEFC. The desired tolerance ability was accomplished by immobilising IrO_x as co-catalyst onto Pt surface through simple electrodeposition method. Immobilising precursor was colloidal suspension of $Ir_2O_3.nH_2O$ which as synthesised from solid K_2IrCl_6. The resultant electrode IrO_x-Pt was electrochemically characterized by means of cyclic voltammetric technique. In ethanol oxidation reaction, Pt showed higher current response, but its CO tolerance ability was almost 3.5 times lower than the IrO_x-Pt electrode. This result is also consistent with stability test of the electrodes in which the activity of Pt declined over 500 incessant cycling and retained just (50±1.53) % current density, whereas the activity of IrO_x-Pt electrode decreased by (18±1.15) % after 500 cycles. As the IrO_x-Pt electrode showed less

susceptibility towards CO adsorption in attaining EtOR, therefore it can also be used as CO-tolerant catalyst in methanol oxidation reaction for direct methanol fuel cell.

Authors contribution

Md. Fahamidul Islam: Writing-original draft, experimental and data analysis, **Jahir Ahmed:** Data analysis, review and editing, and funding acquisition, **M. Faisal:** Review and editing, **Jari S Algethami:** Review and editing, **Kentaro Aoki:** Surface analysis and review, **Yuki Nagao:** Surface analysis and review, **Farid A. Haraz:** Review and editing, supervision, and funding acquisition, **Mohammad A. Hasnat:** Conceptualization, writing-review & editing, supervision, and funding acquisition.

Conflict of interest

There are no conflicts of interest to declare

Acknowledgements

The authors are thankful to the Deanship of Scientific Research at Najran University for funding this work, under the Research Groups Funding Program grant code (NU/RG/SERC/12/17). K.A. and Y.N. are grateful for the research funding of JST CREST Grant Number JPMJCR21B3, Japan. MAH thanks Ministry of education (PS20211727) and University of grant commission-UGC (2022) for their grant.

References

1 A. Kalair, N. Abas, M. S. Saleem, A. R. Kalair and N. Khan, *Energy Storage*, 2021, **3**, e135.
2 L. Chiari and A. Zecca, *Energy Policy*, 2011, **39**, 5026–5034.
3 Climate Change, https://climate.nasa.gov/, (accessed May 19, 2022).
4 Ipcc, *Global Warming of 1.5°C: IPCC Special Report on impacts of global warming of 1.5°C above pre-industrial levels in context of strengthening response to climate change, sustainable development, and efforts to eradicate poverty*, Cambridge University Press, 1st edn., 2022.
5 C. Lamy, S. Rousseau, E. M. Belgsir, C. Coutanceau and J.-M. Léger, *Electrochimica Acta*, 2004, **49**, 3901–3908.
6 R. M. Castagna, J. M. Sieben, A. E. Alvarez, M. D. Sanchez and M. M. E. Duarte, *Materials Today Energy*, 2020, **15**, 100366.
7 J. A. Kruse, *Critical Care Clinics*, 2012, **28**, 661–711.
8 S. Abdullah, S. K. Kamarudin, U. A. Hasran, M. S. Masdar and W. R. W. Daud, *Journal of Power Sources*, 2014, **262**, 401–406.
9 M. A. F. Akhairi and S. K. Kamarudin, *International Journal of Hydrogen Energy*, 2016, **41**, 4214–4228.
10 R. M. C. Silva, G. A. Camara and M. J. Giz, *Electrochimica Acta*, 2019, **308**, 167–173.
11 K. Ding, D. Zhang, J. Li, J. Chen, F. Shi, B. Li, X. He, L. Wang and H. Wang, *International Journal of Hydrogen Energy*, 2022, **47**, 276–291.

12 L. S. R. Silva, C. V. S. Almeida, C. T. Meneses, E. A. Batista, S. F. Santos, K. I. B. Eguiluz and G. R. Salazar-Banda, *Applied Catalysis B: Environmental*, 2019, **251**, 313–325.
13 S. Mohanapriya and D. Gopi, *Renewable and Sustainable Energy Reviews*, 2021, **148**, 111211.
14 K.-U. Lee, J. Y. Byun, H.-J. Shin and S. H. Kim, *Journal of Alloys and Compounds*, 2020, **842**, 155847.
15 N. Xaba, R. M. Modibedi, M. K. Mathe and L. E. Khotseng, *Electrocatalysis*, 2019, **10**, 332–341.
16 S. Roy Chowdhury, J. C. Bhangoji, T. Maiyalagan and S. S. Shendage, *International Journal of Hydrogen Energy*, 2021, **46**, 4036–4044.
17 L. M. Palma, T. S. Almeida and A. R. de Andrade, *Journal of Electroanalytical Chemistry*, 2020, **878**, 114592.
18 S. C. S. Lai and M. T. M. Koper, *Phys. Chem. Chem. Phys.*, 2009, **11**, 10446.
19 Z. Liu, X. Y. Ling, X. Su and J. Y. Lee, *J. Phys. Chem. B*, 2004, **108**, 8234–8240.
20 S. Grigoriev, E. Lyutikova, S. Martemianov and V. Fateev, *International Journal of Hydrogen Energy*, 2007, **32**, 4438–4442.
21 J. Friedl and U. Stimming, *Electrochimica Acta*, 2013, **101**, 41–58.
22 N. Fujiwara, K. A. Friedrich and U. Stimming, *Journal of Electroanalytical Chemistry*, 1999, **472**, 120–125.
23 K. M. Hassan, A. A. Hathoot, R. Maher and M. Abdel Azzem, *RSC Adv.*, 2018, **8**, 15417–15426.
24 W. Du, G. Yang, E. Wong, N. A. Deskins, A. I. Frenkel, D. Su and X. Teng, *J. Am. Chem. Soc.*, 2014, **136**, 10862–10865.
25 Y. Liu, M. Wei, D. Raciti, Y. Wang, P. Hu, J. H. Park, M. Barclay and C. Wang, *ACS Catal.*, 2018, **8**, 10931–10937.
26 M. Li, A. Kowal, K. Sasaki, N. Marinkovic, D. Su, E. Korach, P. Liu and R. R. Adzic, *Electrochimica Acta*, 2010, **55**, 4331–4338.
27 J. Ribeiro, D. M. dos Anjos, K. B. Kokoh, C. Coutanceau, J.-M. Léger, P. Olivi, A. R. de Andrade and G. Tremiliosi-Filho, *Electrochimica Acta*, 2007, **52**, 6997–7006.
28 J. Tayal, B. Rawat and S. Basu, *International Journal of Hydrogen Energy*, 2011, **36**, 14884–14897.
29 E. Ribadeneira and B. A. Hoyos, *Journal of Power Sources*, 2008, **180**, 238–242.
30 Y. Fang, S. Guo, D. Cao, G. Zhang, Q. Wang, Y. Chen, P. Cui, S. Cheng and W. Zuo, *Nano Res.*, 2022, **15**, 3933–3939.
31 F. Maillard, G.-Q. Lu, A. Wieckowski and U. Stimming, *J. Phys. Chem. B*, 2005, **109**, 16230–16243.
32 A. B. Anderson, E. Grantscharova and S. Seong, *J. Electrochem. Soc.*, 1996, **143**, 2075–2082.
33 W. A. Rigdon and X. Huang, *Journal of Power Sources*, 2014, **272**, 845–859.
34 G. M. Alvarenga and H. M. Villullas, *Current Opinion in Electrochemistry*, 2017, **4**, 39–44.
35 H. B. Suffredini, G. R. Salazar-Banda and L. A. Avaca, *Journal of Power Sources*, 2007, **171**, 355–362.
36 L. Cao, G. Sun, H. Li and Q. Xin, *Electrochemistry Communications*, 2007, **9**, 2541–2546.
37 H. Song, S. Zhang, J. Ma and M. Luo, *J. Electrochem. Soc.*, 2022, **169**, 054509.
38 J. Courtois, W. Du, E. Wong, X. Teng and N. A. Deskins, *Applied Catalysis A: General*, 2014, **483**, 85–96.
39 E. Antolini, *CHEMELECTROCHEM*, 2014, **1**, 318–328.
40 M. L. Calegaro, H. B. Suffredini, S. A. S. Machado and L. A. Avaca, *Journal of Power Sources*, 2006, **156**, 300–305.
41 K. Fatih, V. Neburchilov, V. Alzate, R. Neagu and H. Wang, *Journal of Power Sources*, 2010, **195**, 7168–7175.
42 M. A. Hasnat, M. Siddika, S. M. N. Uddin, K. A. Alamry and M. M. Rahman, *Electrochimica Acta*, 2021, **392**, 138999.
43 Md. F. Islam, R. H. Rakib, K. A. Alamry, M. M. Rahman and M. A. Hasnat, *Journal of Electroanalytical Chemistry*, 2022, **907**, 116031.
44 M. Shiozawa, K. Kitazumi, M. Iwai, S. Mizuno, N. Kato, Y. Takeda and T. Hamaguchi, *Electrocatalysis*, 2022, **13**, 830–837.

45 S. Siracusano, N. Van Dijk, E. Payne-Johnson, V. Baglio and A. S. Aricò, *Applied Catalysis B: Environmental*, 2015, **164**, 488–495.
46 G. C. da Silva, N. Perini and E. A. Ticianelli, *Applied Catalysis B: Environmental*, 2017, **218**, 287–297.
47 H.-J. Chao, Z.-S. Lin, M. M. R. Singuru and M.-C. Chuang, *Electrochimica Acta*, 2021, **383**, 138291.
48 Competition and selectivity during parallel evolution of bromine, chlorine and oxygen on IrOx electrodes - ScienceDirect, https://www.sciencedirect.com/science/article/pii/S0021951720301962, (accessed September 12, 2022).
49 D. F. Abbott, D. Lebedev, K. Waltar, M. Povia, M. Nachtegaal, E. Fabbri, C. Copéret and T. J. Schmidt, *Chem. Mater.*, 2016, **28**, 6591–6604.
50 The degradation of Pt/IrOx oxygen bifunctional catalysts - ScienceDirect, https://www.sciencedirect.com/science/article/abs/pii/S0013468619306929, (accessed September 12, 2022).
51 P.-Y. Liu, C.-C. Hsu and M.-C. Chuang, *J. Mater. Chem. A*, 2017, **5**, 2959–2971.
52 S. W. Lee, C. Baik, D.-H. Kim and C. Pak, *Journal of Power Sources*, 2021, **493**, 229689.
53 K. Bhattacharyya, C. Poidevin and A. A. Auer, *J. Phys. Chem. C*, 2021, **125**, 4379–4390.
54 M. Dai, J. Xia, Z. Xue, G. Zhou, D. Jiang, Y. Heng, C. Yu, J. Miao and Q. Li, *Journal of Electroanalytical Chemistry*, 2022, **922**, 116740.
55 J. E. Baur and T. W. Spaine, *Journal of Electroanalytical Chemistry*, 1998, **443**, 208–216.
56 J. F. Rivera, I. Pignot-Paintrand, E. Pereira, B. L. Rivas and J.-C. Moutet, *Electrochimica Acta*, 2013, **110**, 465–473.
57 W. Banerjee, S. Maikap, C.-S. Lai, Y.-Y. Chen, T.-C. Tien, H.-Y. Lee, W.-S. Chen, F. T. Chen, M.-J. Kao, M.-J. Tsai and J.-R. Yang, *Nanoscale Research Letters*, 2012, **7**, 194.
58 B. Jiang, J. Kim, Y. Guo, K. C. W. Wu, S. M. Alshehri, T. Ahamad, N. Alhokbany, J. Henzie and Y. Yamachi, *Catalysis Science & Technology*, 2019, **9**, 3697–3702.
59 R. Kötz, H. Neff and S. Stucki, *J. Electrochem. Soc.*, 1984, **131**, 72.
60 S. Cherevko, S. Geiger, O. Kasian, A. Mingers and K. J. J. Mayrhofer, *Journal of Electroanalytical Chemistry*, 2016, **774**, 102–110.
61 S. Banik, A. Mahajan, S. R. Chowdhury and S. K. Bhattacharya, *RSC Adv.*, 2016, **6**, 92490–92501.
62 J. Hong, Y.-X. Zhao, B.-L. Xiao, A. A. Moosavi-Movahedi, H. Ghourchian and N. Sheibani, *Sensors*, 2013, **13**, 8595–8611.
63 E. Laviron, *Journal of Electroanalytical Chemistry and Interfacial Electrochemistry*, 1974, **52**, 355–393.
64 E. Laviron, *Journal of Electroanalytical Chemistry and Interfacial Electrochemistry*, 1979, **101**, 19–28.
65 C. Xu and P. K. Shen, *Journal of Power Sources*, 2005, **142**, 27–29.
66 Y. Bai, J. Wu, J. Xi, J. Wang, W. Zhu, L. Chen and X. Qiu, *Electrochemistry Communications*, 2005, **7**, 1087–1090.
67 H. B. Suffredini, V. Tricoli, N. Vatistas and L. A. Avaca, *Journal of Power Sources*, 2006, **158**, 124–128.
68 J. C. M. Silva, R. F. B. De Souza, L. S. Parreira, E. T. Neto, M. L. Calegaro and M. C. Santos, *Applied Catalysis B: Environmental*, 2010, **99**, 265–271.
69 D.-J. Guo, *Journal of Power Sources*, 2011, **196**, 679–682.
70 M. Hasan, S. B. Newcomb and K. M. Razeeb, *ECS Trans.*, 2013, **45**, 111–126.
71 Q. He, Y. Shen, K. Xiao, J. Xi and X. Qiu, *International Journal of Hydrogen Energy*, 2016, **41**, 20709–20719.
72 S. Maturost, S. Themsirimongkon, P. Waenkaew, N. Promsawan, J. Jakmunee and S. Saipanya, *International Journal of Hydrogen Energy*, 2021, **46**, 5999–6013.
73 R. M. Antoniassi, J. Quiroz, E. C. M. Barbosa, L. S. Parreira, R. A. Isidoro, E. V. Spinacé, J. C. M. Silva and Pedro. H. C. Camargo, *ChemCatChem*, 2021, **13**, 1931–1939.

74 A. Sandoval-González, J. A. A. Navarro, M. A. Rivera Martínez, F. Paraguay-Delgado and S. A. Gamboa, *International Journal of Hydrogen Energy*, 2022, **47**, 30262–30276.
75 M. A. Hasnat, Z. Mumtarin and M. M. Rahman, *Electrochimica Acta*, 2019, **318**, 486–495.
76 R. M. Abdel Hameed, *Journal of Colloid and Interface Science*, 2017, **505**, 230–240.
77 W. Wang, X. Liu, Y. Wang, L. Zhang, S. Imhanria and Z. Lei, *Journal of the Taiwan Institute of Chemical Engineers*, 2019, **104**, 284–292.
78 C. R. Santiago-Ramírez, J. Vera-Iturriaga, P. del Angel, A. Manzo-Robledo, M. L. Hernández-Pichardo and J. Soto-Hernández, *Applied Catalysis B: Environmental*, 2021, **282**, 119545.